D. Bellora, R. Vescovini
Hybrid Geometric-Dissipative Arc-Length Methods for the Quasi-Static Analysis of Delamination Problems
Computers & Structures, Vol. 175, 2016, p. 123-133
doi:10.1016/j.compstruc.2016.07.002

Hybrid Geometric-Dissipative Arc-Length Methods for the Quasi-Static Analysis of Delamination Problems

Davide Bellora and Riccardo Vescovini[1]

Department of Aerospace Science and Technology, Politecnico di Milano
Via La Masa 34,
20156 Milano, Italy

Abstract

This paper presents a class of arc-length methods for the quasi-static analysis of problems involving material and geometric nonlinearities. A constraint equation accounting for geometric and dissipative requirements is adopted: the geometric part refers to the Riks and Crisfield equations, while the dissipative one refers to the dissipated energy. The approach allows for a continuous variation of the nature of the constraint, and a switch criterion is not needed to trace the elastic and the dissipative parts of the equilibrium paths. To illustrate the robustness and the efficiency of the methods, three examples with geometric and material nonlinearities are discussed.

Keywords: Delaminations, Arc-length methods, Cohesive elements, Numerical methods.

1. Introduction

Arc-length techniques are numerical solution strategies that can successfully handle structural responses characterized by limit points. Pioneering work in this field is due to Riks [1] and Wempner [2], which introduced the idea of adding a load parameter, and consequently a contraint equation, as additional unknown of the problem. In these procedures, the load is free to increase or decrease throughout the iterative process, and the singularities of Jacobian matrix at the turning points are removed.
Further developments of the arc-length methods have been proposed in the early eighties. Ramm

[1]Corresponding author. *Email address:* riccardo.vescovini@polimi.it (Riccardo Vescovini)

developed the updated normal path method [3], imposing the orthogonality between the iterative and the total increments. Crisfield [4] proposed a modified implementation of the arc-length solution scheme, focusing on the finite element implementation of the method and aiming to preserve the symmetric-banded nature of the equilibrium equations. This method is sometimes denoted as the spherical arc-length and the corresponding constraint equation is quadratic. A modified procedure was successively presented by the same author, based on the observation that material nonlinearities may determine convergence issues when faced with standard arc-length procedure. To this aim, a line search algorithm was introduced in the solution process [5]. A comprehensive review of the arc-length methods is provided in [6]. In general, arc-length strategies are well suited to solve nonlinear elastic problems, but they are likely to suffer from convergence issues in presence of material softening [7, 8]. In presence of delamination phenomena, the strain field is characterized by high localization in a restricted area surrounding the crack tip. It follows that the typical constraint equation based on global quantities tends to fail in capturing the process. To overcome this problem, the so-called local arc-lengths have been proposed by many authors [8, 9, 10]. The idea of these methods is to consider constraint equations based on the displacements of the dominant nodes, i.e. those nodes involved in the delamination process. In the implemenation proposed by de Borst [11], the sliding displacement of a crack was adopted, while Rots and De Borst [12] considered the opening of the crack. May and Duan proposed the use of the relative displacement in the regions undergoing highly nonlinear processes [8]. In the work of Alfano and Crisfield [13], the control function is obtained as a weighted sum of a localized set of relative-displacement parameters.

In Ref. [14] a solution procedure is developed to study the delamination propagation based on the linear elastic fracture mechanics and Virtual Crack Propagation Tehcnique (VCCT). The delamination length is used as the constraint variable, and the load increment size is controlled by means of the energy release rate. Despite the robustness of the local arc-lengths methods, the main drawback is that a priori knowledge of the failure process zone is needed, as the local degrees of freedom entering the constraint equation need to be identified. This restriction can be solved by adopting a path following constraint based on the energy release rate, as proposed by Gutierrez [15] and Verhoosel et al. [16]. This approach allows to develop robust methods, able to describe complex structural responses involving geometric and material nonlinearities. In any case, a double solution strategy is needed to switch from the elastic and the dissipative phases, as the dissipated energy is null during the elastic loading phases. A relevant aspect is then the criterion to handle the transition from the dissipative to the elastic solution procedure. In Refs.

[15, 16], the dissipative part is solved by considering a constraint based on the energy release rate, while the elastic phase is solved with a force control, activated on the basis of an energy threshold value. A first drawback of this strategy relies in the number of iterations, and the consequent impact on the efficiency of the method, characterizing the switch from the dissipative to the elastic solution procedure. A second restriction is the inability of the force-control to tackle responses characterized by purely elastic unloading phases, such as in the cases of snap-through or snap-back phenomena.

In this paper, a class of methods, hereinafter denoted as hybrid-methods, is presented. The methods are based on the combined use of geometric and dissipative constraint equations, which are updated at each step of the solution process on the basis of the damage state of the structure. Goal of these procedures is to guarantee robustness and improved computational efficiency, avoiding abrupt time-consuming transitions between the solution strategies for the dissipative and the elastic phase.

Preliminary aspects of the arc-length solution procedures are reviewed in Section 2, and the main features of the hybrid methods are presented in Section 3. The equations describing the hybrid-Riks method are derived in Section 3.1, while the Crisfield version is proposed in Section 3.2 together with a novel technique for the root selection of the quadratic constraint equation. The application of the hybrid-methods to three numerical examples is discussed in Section 4, where the performance is discussed in terms of robustness and computational efficiency.

2. Preliminaries on the Arc-Length Methods

The finite element approximation of the nonlinear structural problem can be represented by the following set of discrete equilibrium equations:

$$\mathbf{f}_{int}\big(\mathbf{a}\big) = \mathbf{f}_{ext} \tag{1}$$

where the vectors $\mathbf{f}_{int}$ and $\mathbf{f}_{ext}$ denote the internal forces and the applied loads, respectively. The vector $\mathbf{a}$ collects the degrees of freedom of the problem and, in the context of a displacement-based approach, they coincide with the nodal displacements. The set of equations of Eq. (1) is often solved with a force-control, meaning that the load is progressively increased, starting from the unloaded configuration, in the context of Newton-like iterations. In this case, unloading paths cannot be captured. This restriction can be avoided if a displacement-based control is conducted, consisting in specifying, step by step, the imposed value of the displacements at a given set of nodes. This approach can be applied to analyze a wide range of structural problems,

but is not adequate to trace the full equilibrium path in those cases characterized by snap-backs. To overcome the limitations related to the incremental solution procedures, the arc-length methods can be successfully adopted. These approaches are based on the representation of the external load as the product between a vector defining the shape of the load set, $\hat{\mathbf{f}}$, and a scalar parameter λ which determines the magnitude of the load. The load factor λ is then part of the problem unknowns, and its value is free to increase or decrease during the solution procedure. The presence of the additional unknown λ makes the system of Eq. (1) underdetermined, and one further equation, i.e. the constraint equation, is needed. The structural problem is then formulated as:

$$\begin{cases} \mathbf{f}_{int}(\mathbf{a}, \lambda) - \lambda \hat{\mathbf{f}} = 0 \\ g(\mathbf{a}, \lambda) = 0 \end{cases} \tag{2}$$

where the second term is a scalar equation defining the constraint.

The augmented system of Eq. (2) is usually solved by means of a predictor-corrector scheme. In the first step, the predictor provides an approximate solution. In the second step, the corrector phase, the predictor solution is used as the initial guess for an iterative procedure based on the Newton-Raphson method.

The problem unknowns of Eq. (2) are decomposed as:

$$\Delta\mathbf{a} = \Delta\mathbf{a}_j + d\mathbf{a} \ , \qquad \Delta\lambda = \Delta\lambda_j + d\lambda \tag{3}$$

where $\Delta\mathbf{a}$ and $\Delta\lambda$ denote the total increments at the current step, $\Delta\mathbf{a}_j$ and $\Delta\lambda_j$ are the increments at the last iteration j, and $d\mathbf{a}$ and $d\lambda$ are the increments referred to the current iteration (corresponding to the index $j+1$). The index $j = 0$ denotes the predictor solution, while the values $j = 1, \ldots, N$ define the corrector iterations. A graphical representation of Eq. (3) is reported in Figure 1, where the iterations of the Newton's method and the related increments of the unknowns are reported for a single load step.

By application of the Newton-Raphson method to Eq. (1), the following linearized set of equations is obtained:

$$\begin{cases} \mathbf{K} d\mathbf{a} - d\lambda \hat{\mathbf{f}} = \mathbf{r} \\ \mathbf{h}^T d\mathbf{a} + w d\lambda = -g_j \end{cases} \tag{4}$$

where:

$$\mathbf{K} = \frac{\partial \mathbf{f}_{int}}{\partial \mathbf{a}}, \quad \mathbf{h}^T = \frac{\partial g}{\partial \mathbf{a}}, \quad w = \frac{\partial g}{\partial \lambda}, \quad g_j = g\big(\Delta\mathbf{a}_j, \Delta\lambda_j\big) \tag{5}$$

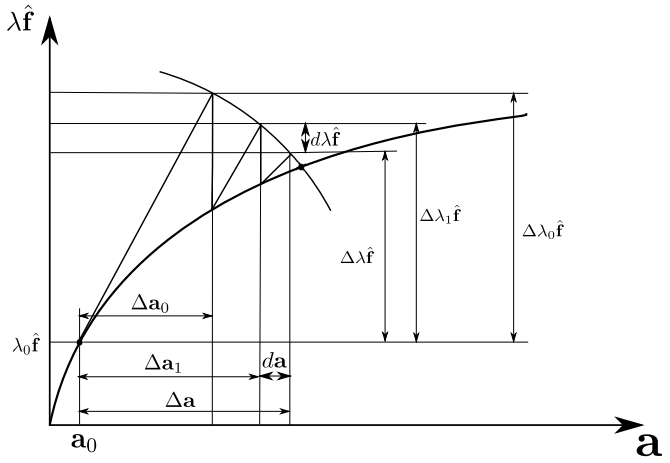

Figure 1: Graphical representation of the decomposition of the unknowns.

and the residual $\mathbf{r}$ is defined as:

$$\mathbf{r} = \Delta\lambda_j\hat{\mathbf{f}} - \mathbf{f}_{int}(\Delta\mathbf{a}_j, \Delta\lambda_j) \tag{6}$$

The system of Eq. (4) can be solved by substitution, so that the iterative increments $d\mathbf{a}$ and $d\lambda$ are derived as:

$$\begin{aligned} d\mathbf{a} &= \mathbf{a}_I + d\lambda\mathbf{a}_{II} \\ d\lambda &= -\frac{g_j + \mathbf{h}^T\mathbf{a}_{II}}{\mathbf{h}^T\mathbf{a}_I + w} \end{aligned} \tag{7}$$

where:

$$\mathbf{a}_I = \mathbf{K}^{-1}\hat{\mathbf{f}} \qquad \mathbf{a}_{II} = \mathbf{K}^{-1}\mathbf{r} \tag{8}$$

After substituting Eq. (7) into Eq. (3), the total increment of the current step can be determined. Traditional arc-length methods – two examples are given by the Riks [1] and the Crisfield [4] formulations – are based on constraint equations that prescribe a geometric relation between the applied loads and the increments of the displacement vector. For the Riks method, the orthogonality is imposed between the iterative increment $d\mathbf{a}$, computed with the corrector, and the displacement increment $\Delta\mathbf{a}_0$, computed with the predictor. In this case, the constraint equation reads:

$$g(\Delta\mathbf{a}, \Delta\lambda) = \Delta\mathbf{a}_0^T d\mathbf{a} = 0 \tag{9}$$

In the strategy proposed by Crisfield, the equilibrium solution is constrained to fall at the intersection between the equilibrium path and a hypersphere of radius Δl centered in the last

computed equilibrium point. In this case, the constraint equation is:

$$g(\Delta\mathbf{a}, \Delta\lambda) = \Delta\mathbf{a}^T \Delta\mathbf{a} + \Delta\lambda^2 \hat{\mathbf{f}}^T \hat{\mathbf{f}} - \Delta l^2 = 0 \tag{10}$$

It is important to remark that the arc-length strategies based on geometric constraints are suitable for the solution of problems dominated by geometric nonlinearities. On the other hand, they can be subjected to convergence issues when applied to problems involving material softening [17]. To overcome this limitations, specific arc-length techniques have been developed in the past. The dissipated energy (DE) arc-length methods developed by Gutierrez [15] and Verhoosel and co-workers [16] are based on the adoption of a dissipative constraint in the form:

$$g(\Delta\mathbf{a}, \Delta\lambda) = \frac{1}{2}\big(\lambda_0 \Delta\mathbf{a}^T - \Delta\lambda \mathbf{a}_0^T\big)\hat{\mathbf{f}} - \Delta\tau = 0 \tag{11}$$

where $[\mathbf{a}_0, \lambda_0]$ is the last converged equilibrium point and $\Delta\tau$ is the dissipated energy.
The constraint of Eq. (11) prescribes the amount of energy dissipation at the current load step, which has the advantage of being always positive, since τ is a monotonically increasing quantity during the damage process. However, the constraint can be used to trace only the dissipative parts of the equilibrium path, while a different strategy is needed for the elastic loading phase. Following the implementation of Ref. [16], a force-control can be activated when the dissipation increment is smaller than a threshold value. This strategy will be denoted in the next as Dissipated Energy method (DE).

3. The Hybrid-Constraint Methods

Goal of the hybrid-constraint techniques is to provide an automated, improved, strategy to properly handle the transition between geometric and dissipative constraint equations, overcoming the restrictions due to the use of a force-control incrementation. These techniques aim to facilitate the analysis of a wide class of problems, including those dominated by geometric nonlinearities, strain-softening responses, elastic and dissipative unloading phases. Based on these considerations, the constraint equation, in its general form, is expressed as:

$$g(\Delta\mathbf{a}, \Delta\lambda) = \big(1 - \gamma\big)\, c(\Delta\mathbf{a}, \Delta\lambda) + \gamma\, h(\Delta\mathbf{a}, \Delta\lambda) \tag{12}$$

where $\gamma \in [0, 1]$ is a weighting function, whose value is updated at the end of each step; $c(\Delta\mathbf{a}, \Delta\lambda)$ denotes the generic geometric constraint, while $h(\Delta\mathbf{a}, \Delta\lambda)$ is the dissipative one. The former can be taken as the equations derived by Riks and Crisfield (see Eqs. (9) and (10)), the latter

is the constraint accounting for material dissipation and, as an example, it can be taken in the form of Eq. (11).
The expression of Eq. (12) defines a family of constraint equations: by combining different geometric and dissipative constraints, as well as by adopting different expressions of the weighting function, a wide number of methods could ideally be generated.
The choice of the weight function γ of Eq. (12) is a crucial step in the development of the hybrid-methods. Indeed, it strongly influences the performance of the procedure, as it is responsible for handling the transition between the geometric and the dissipative constraint. A proper definition of the function should account for the following three features:

- Be close to zero in absence of dissipation phenomena, when the response is purely elastic
- Display a rate of growth proportional to the intensity of the dissipation phenomena
- Approach the unitary value as the problem becomes dissipation-driven

As far as the weighting function should exhibit a certain degree of sensitivity to the damage state of the structure, the damage variable d of the cohesive elements is here considered as the free parameter of γ. The quantity d satisfies the three requirements previously mentioned and, by the definition, is bounded in the interval [0, 1]. Based on a wide set of preliminary tests, a suitable choice to achieve robust algorithms is obtained by setting γ equal to the maximum non-unitary value of d, i.e.:

$$\gamma = \max\{d : d \neq 1\} \tag{13}$$

It is important to highlight that the maximum is taken, at each step, among the damage variables of the cohesive elements, excluding those equal to 1. This criterion is implemented to avoid that the weight γ remains unitary for the total duration of the simulation once that one single fully damaged element is present in the model. The dependency of the weighting function on the damage variable implies that the method can be applied only if the finite element model makes use of cohesive elements for the prediction of the crack onset and propagation.
Two distinct implementations of the hybrid-constraint algorithms are here proposed, the hybrid-Riks and the hybrid-Crisfield methods. The two methods are obtained by combining different geometric constraints, the Riks and Crisfield equations, while in both cases the dissipative constraint is based on Eq. (11).

3.1. The Hybrid-Riks Method

The hybrid-Riks method is obtained by substitution of the Riks and the dissipative equations, i.e. Eqs. (9) and (11), into the hybrid-method constraint of Eq. (12). The expression becomes:

$$g(\Delta\mathbf{a},\Delta\lambda) = (1-\gamma)\big(\Delta\mathbf{a}_0^T d\mathbf{a}\big) + \gamma\Big(\frac{1}{2}\lambda_0\Delta\mathbf{a}^T\hat{\mathbf{f}} - \frac{1}{2}\Delta\lambda\mathbf{a}_0^T\hat{\mathbf{f}} - \Delta\tau\Big) \tag{14}$$

It is worth observing that Eq. (14) is linear, as it is derived from Eqs. (9) and (11). It follows that one single set of values $[\Delta\mathbf{a},\Delta\lambda]$ defines the solution of the system of Eq. (2) at each step. Referring to Eq. (4), the equilibrium configuration is obtained by solving the following linearized system:

$$\begin{cases} \mathbf{K}d\mathbf{a} - d\lambda\hat{\mathbf{f}} = \mathbf{r} \\ (1-\gamma)\big(\Delta\mathbf{a}_0^T d\mathbf{a}\big) + \gamma\Big(\frac{1}{2}\lambda_0\Delta\mathbf{a}^T\hat{\mathbf{f}} - \frac{1}{2}\Delta\lambda\mathbf{a}_0^T\hat{\mathbf{f}} - \Delta\tau\Big) = 0 \end{cases} \tag{15}$$

After substitution of Eq. (3) in the linearised system of Eq. (15), the governing equations become:

$$\begin{cases} \mathbf{K}d\mathbf{a} - d\lambda\hat{\mathbf{f}} = \mathbf{r} \\ \Big((1-\gamma)\Delta\mathbf{a}_0^T + \frac{1}{2}\gamma\lambda_0\hat{\mathbf{f}}^T\Big)d\mathbf{a} - \frac{1}{2}\gamma\mathbf{a}_0^T\hat{\mathbf{f}}d\lambda + \frac{1}{2}\gamma\lambda_0\Delta\mathbf{a}_j^T\hat{\mathbf{f}} - \frac{1}{2}\gamma\Delta\lambda_j\mathbf{a}_0^T\hat{\mathbf{f}} - \gamma\Delta\tau = 0 \end{cases} \tag{16}$$

The iterative solutions of Eq. (16) are derived by solving the system of equations by substitution, which gives:

$$\begin{aligned} d\mathbf{a} &= \mathbf{a}_I + d\lambda\mathbf{a}_{II} \\ d\lambda &= -\frac{\tilde{b_2}}{\tilde{b_1}} \end{aligned} \tag{17}$$

where $\mathbf{a}_I$ and $\mathbf{a}_{II}$ are defined by Eq. (8) and:

$$\begin{aligned} \tilde{b_1} &= (1-\gamma)\big(\Delta\mathbf{a}_0^T\mathbf{a}_I\big) + \gamma\Big(\frac{1}{2}\lambda_0\mathbf{a}_I^T\hat{\mathbf{f}} - \frac{1}{2}\mathbf{a}_0^T\hat{\mathbf{f}}\Big) \\ \tilde{b_2} &= (1-\gamma)\big(\Delta\mathbf{a}_0^T\mathbf{a}_{II}\big) + \gamma\Big(\frac{1}{2}\lambda_0\Delta\mathbf{a}_j^T\hat{\mathbf{f}} + \frac{1}{2}\lambda_0\mathbf{a}_{II}^T\hat{\mathbf{f}} - \frac{1}{2}\Delta\lambda_j\mathbf{a}_0^T\hat{\mathbf{f}} - \Delta\tau\Big) \end{aligned} \tag{18}$$

3.2. The Hybrid-Crisfield Method

A second version of the solution techniques here developed is the hybrid-Crisfield method, which is based on the combination of the Crisfield and the dissipated energy constraints. After substituting Eqs. (10) and (11) into Eq. (12), the constraint equation is obtained as:

$$g(\Delta\mathbf{a},\Delta\lambda) = (1-\gamma)\big(\Delta\mathbf{a}^T\Delta\mathbf{a} + \Delta\lambda^2\hat{\mathbf{f}}^T\hat{\mathbf{f}} - \Delta l^2\big) + \gamma\Big(\frac{1}{2}\lambda_0\Delta\mathbf{a}^T\hat{\mathbf{f}} - \frac{1}{2}\Delta\lambda\mathbf{a}_0^T\hat{\mathbf{f}} - \Delta\tau\Big) \tag{19}$$

It is highlighted that the constraint of Eq. (19) is quadratic in $\Delta\mathbf{a}$ and $\Delta\lambda$, as it is derived from the combination of a quadratic equation, Eq. (10), and a linear equation, Eq. (11). Therefore, two solutions exist at each step, and a criterion for the root selection is needed.
Adopting Eq. (19) as the constraint equation, the linearized system of Eq. (4) reads:

$$\begin{cases} \mathbf{K}d\mathbf{a} - d\lambda\hat{\mathbf{f}} = \mathbf{r} \\ (1-\gamma)\big(\Delta\mathbf{a}^T\Delta\mathbf{a} + \Delta\lambda^2\hat{\mathbf{f}}^T\hat{\mathbf{f}} - \Delta l^2\big) + \gamma\Big(\frac{1}{2}\lambda_0\Delta\mathbf{a}^T\hat{\mathbf{f}} - \frac{1}{2}\Delta\lambda\mathbf{a}_0^T\hat{\mathbf{f}} - \Delta\tau\Big) = 0 \end{cases} \tag{20}$$

Introducing Eq. (3) in the system of Eq. (20), it is obtained:

$$\begin{cases} \mathbf{K}d\mathbf{a} - d\lambda\hat{\mathbf{f}} = \mathbf{r} \\ (1-\gamma)\big((d\mathbf{a}^T d\mathbf{a} + 2\Delta\mathbf{a}_j^T d\mathbf{a} + \Delta\mathbf{a}_j^T\Delta\mathbf{a}_j) + (d\lambda^2 + 2\Delta\lambda_j d\lambda + \Delta\lambda_j^2)\hat{\mathbf{f}}^T\hat{\mathbf{f}} - \Delta l^2\big) + \\ \quad +\gamma\Big(\frac{1}{2}\lambda_0\hat{\mathbf{f}}^T(d\mathbf{a} + \Delta\mathbf{a}_j) - \frac{1}{2}(d\lambda + \Delta\lambda_j)\mathbf{a}_0^T\hat{\mathbf{f}} - \Delta\tau\Big) = 0 \end{cases} \tag{21}$$

and solving the system of Eq. (21) by substitution, the iterative solutions $d\mathbf{a}$ and $d\lambda$ are obtained as:

$$d\mathbf{a} = \mathbf{a}_I + d\lambda\mathbf{a}_{II} \tag{22}$$

$$d\lambda = \frac{-c_2 \pm \sqrt{c_2^2 - 4c_1c_3}}{2c_1} \tag{23}$$

where the terms c_i are reported in the Appendix.
It is useful to discuss the geometric interpretation of the method in order to gather insight into the role played by the hybrid constraint equation during the solution process. By assuming one single degree of freedom, the constraint equation of Eq. (19) can be seen as a circumference in the plane $\Delta a - \Delta\lambda$ whose radius R is obtained as:

$$R = \sqrt{\frac{1}{4}\left(\frac{1}{2}\,\frac{\gamma}{1-\gamma}\lambda_0\hat{f}\right)^2 + \frac{1}{4}\left(-\frac{1}{2}\,\frac{\gamma}{1-\gamma}a_0\hat{f}\right)^2 + \Delta l^2 + \frac{\gamma}{1-\gamma}\Delta\tau} \tag{24}$$

The coordinates of the circumference center are:

$$[a_c, \lambda_c] = \Big[-\frac{1}{4}\,\frac{\gamma}{1-\gamma}\lambda_0\hat{f}\,,\ \frac{1}{4}\,\frac{\gamma}{1-\gamma}a_0\hat{f}\Big] \tag{25}$$

As seen from Eqs. (24) and (25), both the radius and the coordinates of the center are function of the weight parameter γ and the last computed equilibrium point. The radius R depends also on the step sizes Δl and $\Delta\tau$. In Figure 2 the circumferences are traced for four different values

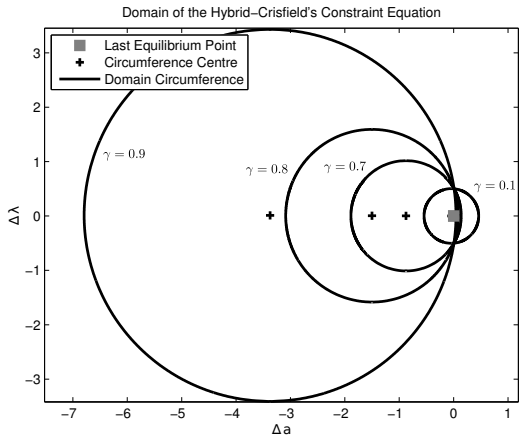

Figure 2: Influence of γ on the domain circumference.

of γ, with $\Delta l = 0.5$, $\Delta\tau = 0.005$, $a_0 = 0.005$, $\lambda_0 = 1.5$, $\hat{f} = 1$.
The graphical representation of Figure 2 illustrates that an increase of the value assumed by γ determines an increase of the radius R. When $\gamma = 0$, the constraint is purely geometric, and represents the circumference of Eq. (10), which is centered in the last equilibrium point and its radius is Δl. Contrarily, when γ approaches the unitary value, the radius R tends to infinity and the circumference tends to the straight line represented by Eq. (11).
Higher values of γ determine a progressive modification of the circumference shape, resulting in an increase of its radius and a shift of the center coordinates, all of them tending to infinity. In practice, the straight line condition is never met, as Eq. (13) cannot assume unitary values by definition.

Energy-Based Root Selection Technique

As far as the constraint of Eq. (19) is quadratic, the method requires the adoption of a criterion for the selection of the root. Among the strategies available in the literature, one possibility is given by the increment direction method. This approach consists in choosing the incremental displacement vector $\mathbf{\Delta a}$ that forms the smallest angle with the vector $\mathbf{\Delta a}$ computed at the previous load step [18]. Despite its effectiveness, the method is likely to determine the doubling back of the solution in correspondence of sharp snap-backs. To overcome this limitation, a second strategy, the so-called lowest residual method has been proposed by Crisfield and Hellweg

[19]. In this case, the main idea is to select, in the neighborhood of a snap-back, the solution with the lowest norm of the residual. The number of operations to compute the residuals of the two solutions suggests to restrict the adoption of the criterion in the surroundings of the snap. Furthermore, a number of preliminary tests demonstrated that for relatively complex structures, such as the perforated cantilever beam, or in the presence of diffused damaged cohesive elements, the method may converge to a solution associated with an unexpected reduction of the load level and a corresponding interruption of the propagation.
For this reason, a novel approach is here proposed for the selection of the root. A brief summary of the pseudo-code is provided in Algorithm 1.

Algorithm 1 Energy-based root selection technique

```
if γ ≤ W_switch then
    Apply Increment direction method
else if γ > W_switch then
    Compute Δτ1, Δτ2
    if Δτ1Δτ2 < 0 then
        Keep solution associated with Δτ > 0
    else if Δτ1Δτ2 > 0 then
        Apply Lowest residual method
    end if
end if
```

The technique combines different root selection methods. The increment direction method is adopted when the weighting parameter is below the threshold W_{switch}, meaning that the equilibrium path is primarily elastic. In presence of dissipative phenomena, whose trigger is defined by the threshold W_{switch}, the selection criterion is based on the analysis of the energy dissipation associated with the two roots of the quadratic equation. In particular, the dissipated energy is obtained as:

$$\Delta\tau_k = \frac{1}{2}\big(\lambda_0 \Delta\mathbf{a}_k^T - \Delta\lambda_k \mathbf{a}_0^T\big)\hat{\mathbf{f}} \qquad (k = 1, 2) \tag{26}$$

where k is the index defining the two roots, and $[\mathbf{a}_0, \lambda_0]$ is the vector of the degrees of freedom at the last converged equilibrium point.
Once the two values of $\Delta\tau_k$ are available, the choice of the solution depends on the sign of the roots. In most cases, they are characterized by different sign, thus allowing for a straightforward selection of the actual solution: due to the irreversibility of the damage process, the only feasible solution is the one relative to a positive dissipation.
Solutions with values of $\Delta\tau$ with the same sign are typically found in the neighborhood of sharp

snap-backs and, in such cases, the root with the lowest norm of the residual, i.e. the closest to equilibrium, is chosen.
The main advantage of the energy-based increment method is the guarantee of convergence to the dissipative solution, thus preventing solutions characterized by an undesired interruption of the damage propagation. Furthermore, the computation of Eq. (26) can be performed with a reduced effort, with a beneficial effect on the overall efficiency of the solution procedure.

4. Numerical Examples

The performance of the hybrid-constraint methods is assessed by means of three numerical examples involving material and geometric nonlinearities. The comparison is presented between the results obtained with the two solution procedures here developed, the hybrid-Riks (HRi) and hybrid-Crisfield (HC) methods, and two techniques available in the literature, the Riks arc-length and the dissipated energy (DE) methods. The reason for choosing the Riks method is due to the better performances we observed, for the examples here discusses, with respect to those obtained using the standard Crisfield method. In this context, it can be mentioned that the minimum-residual variant of the Crisfield method [20] could be another option to perform the benchmarking of the results.
The comparison is discussed in terms of robustness, intended as the ability of the method not to undergo premature failures due to convergence issues, and efficiency, measured as the total time to perform the analysis.
The analyses are performed with the open source finite element code PyFEM [18] and four node, nonlinear, two-dimensional continuum elements are used to model the structure (FiniteStrain-Continuum elements of PyFEM). The mixed-mode cohesive element developed by Camanho et al. [21] was implemented in the code and is here used to capture delaminations.
In all the numerical examples, preliminary convergence studies were carried out to determine the size of the elements. As far as the mesh density is usually dictated by cohesive elements, it was ensured that the size of the elements is smaller than the length of the process zone, estimated as [22, 23]:

$$l_p = \gamma \frac{E G_c}{N^2} \tag{27}$$

where γ is a scalar nondimensional parameter, here taken as 0.884, E denotes the Young's modulus, G_c is the fracture toughness in mode I, and N is the interfacial strength.
Similarly, the numerical parameters of the various algorithms were chosen on the basis of an

extensive set of preliminary analyses aiming to identify the set of input parameters guaranteeing the best performance of the method.
The termination of the analyses is controlled with a global criterion based on the norm of the residual, which is expressed as:

$$\frac{\|\mathbf{r}\|}{\|\lambda\hat{\mathbf{f}}\|} < \text{tol} \tag{28}$$

Following Ref. [18], a secant predictor is implemented in all the hybrid-constraint methods. The strategy consists in extrapolating the increments of the unknowns computed at the previous step using a linear approximation. The predictor solution is then:

$$\begin{aligned} \Delta\mathbf{a}_0^{t+\Delta t} &= \xi\Delta\mathbf{a}^t \\ \Delta\lambda_0^{t+\Delta t} &= \xi\Delta\lambda^t \end{aligned} \tag{29}$$

where the parameter ξ is a scalar multiplier, and the superscripts t and $t+\Delta t$ identify the quantities at previous and the current load steps, respectively.
The multiplier ξ is estimated as:

$$\xi = \left(\frac{N_d}{N_t}\right)^{\zeta} \tag{30}$$

where N_d and N_t are the number of desired iterations at the current load step and those relative to the previous iteration. The parameter ζ is set to 0.5.
All the tests are performed using a laptop with a processor Intel Core i7 1.73 GHz and 4 GB of RAM.

Double Cantilever Beam

The first example deals with the simulation of a double cantilever beam (DCB). Goal of the investigation is to assess the performance of the methods for a standard benchmark case. It is important to remark that the response of the DCB involves a softening behaviour due to the crack onset and propagation. While snap-backs and oscillating behaviours can characterize the response of the DCB (see, for instance, [24]), in the case here discussed the response is relatively smooth. It follows that convergence issues are not expected, even in the context of standard arc-length methods.
The DCB specimen is reported in Figure 3.
It is a beam of length L and width h, divided into two parts along a common interface. An initial crack of length a is introduced. The structure is fixed at one end, and is loaded at the other side with two concentrated forces F.

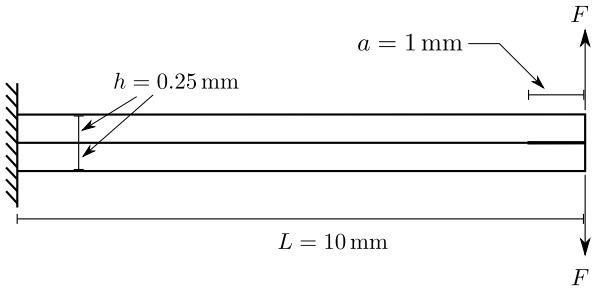

Figure 3: DCB: structural model.

The beam is made of isotropic material with Young's modulus equal to 100 MPa and Poisson's ratio 0.3; plane strain constitutive law is assumed. The properties of the cohesive law are reported in Table 1, where G_I denotes the fracture toughness in mode I, N is the interlaminar strength in mode I and k_d is the penalty stiffness.

G_I (Nmm^{-1})	N (N)	k_d (Nmm^{-3})
$1.0 \cdot 10^{-1}$	1.0	$1.0 \cdot 10^{2}$

Table 1: DCB - properties of the cohesive constitutive law.

The finite element model is shown in Figure 4. In particular, the beam is modeled with 160 two-dimensional continuum elements, and 36 cohesive elements at the interface between the two parts. The initial crack is simulated by introducing a discontinuity between the elements of the upper and the lower part of the beam by means of multiple coincident nodes.

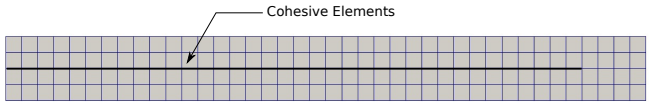

Figure 4: DCB: finite element mesh.

The analyses are performed using the parameters of Table 2, where $\Delta\lambda_0$, Δl_0 and $\Delta\tau_0$ denote the initial values of $\Delta\lambda$, Δl and $\Delta\tau$.
Referring to Eq. (28), a tolerance of $3.0 \cdot 10^{-2}$ is set for all the methods, while the maximum value of the parameter ξ of Eq. (30) is fixed to 1.0. The simulations are terminated when $\lambda \geq 30$. The results of the analysis are presented in Figure 5 in terms of vertical displacement of the

Method	$\Delta\lambda_0$	Δl_0 (mm)	Δl_{max} (mm)	$\Delta\tau_0$ (Nmm)	$\Delta\tau_{max}$ (Nmm)	ξ_{max}	W_{switch}
HRi	1.0	-	-	-	$1.0{\cdot}10^{-2}$	1.0	-
HC	0.05	0.1	0.1	-	$1.0{\cdot}10^{-2}$	1.0	1.0
DE	0.2	-	-	$1.0{\cdot}10^{-3}$	$2.0{\cdot}10^{-3}$	-	-
Riks	5.0	-	-	-	-	1.0	-

Table 2: DCB - analysis parameters.

upper loaded node versus the applied load for the four analysis procedures here investigated. The deformed configuration corresponding to a vertical displacement of 3.06 mm is reported in Figure 6.

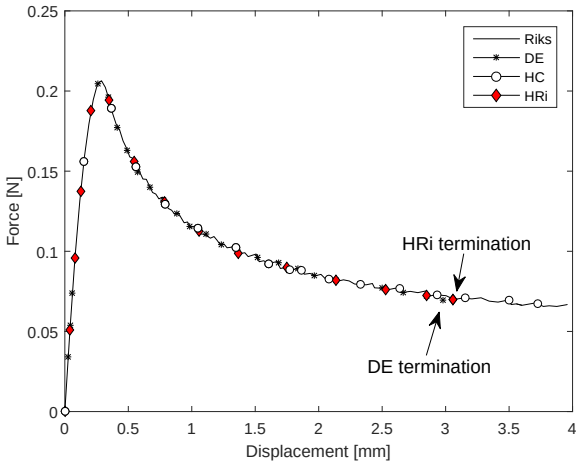

Figure 5: DCB: comparison of the results.

The numerical performances of the methods are summarized in Table 3 in terms of number of steps, iterations and step size reductions, CPU time and maximum computed displacement.
As a metric to assess the robustness of the methods, the vertical displacement is taken as the reference quantity: the higher the vertical displacement, the greater the robustness of the method. As observed from Table 3, the Riks method guarantees a satisfying response in terms of robustness. In the present example, the method is able to reach the convergence until a maximum displacement of 3.96 mm, more than 30% higher than its hybrid counterpart. Similarly, the HC method demonstrates good robustness properties, allowing the simulation to converge until

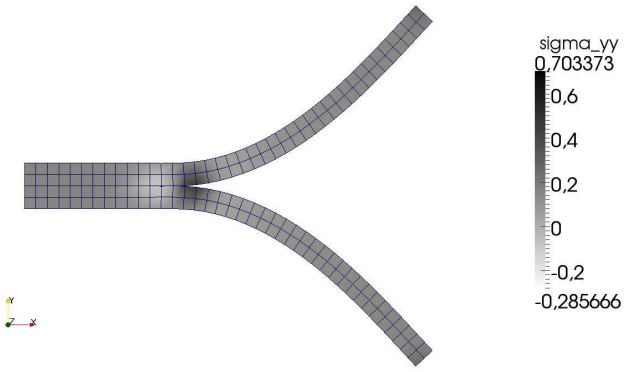

Figure 6: DCB: final deformed configuration.

Method	N. of Incr.	N. of Iter.	N. of Cutbacks	Max. Disp. (mm)	CPU Time (s)
HRi	70	193	8	3.06	150
HC	79	174	15	3.96	139
DE	249	413	1	2.98	385
Riks	110	233	2	3.96	192

Table 3: DCB - numerical performances.

3.96 mm of maximum displacement.

It is interesting to highlight the performance of the HRi method with respect to the DE. While the maximum displacement reached by the two methods is almost the same – and approximately equal to 3 mm -, the time to complete the analysis of the HRi is much smaller, 150 s versus 384 s. Indeed, the DE method requires a small step size to avoid any premature stop and, as a consequence, a high number of load steps is necessary.

In this test, the hybrid-constraint methods do not provide significant advantages with respect to the traditional arc-length strategies. As a matter of fact, the DCB response does not present sharp snap-backs and high damage localization, therefore standard arc-length implementations can be successfully applied. Despite that, the hybrid version of the Riks method still provides a satisfactory behaviour, with convergence properties not too far from those obtained with the Riks method.

Variable-Thickness Double Cantilever Beam

In this example, the propagation of a mode I delamination is investigated for a DCB specimen with a non-uniform width profile. The presence of a variable thickness determines a fluctuating crack propagation speed, and leads to the coexistence of a strain-softening behaviour in conjunction with multiple snap-backs. Aim of the present simulation is to assess the potential gains offered by the use of the hybrid methods when the structural response is characterized by the above mentioned interactions between geometric and material nonlinearities.
The structure consists of two horizontal parts separated by an interface, as illustrated in Figure 7.

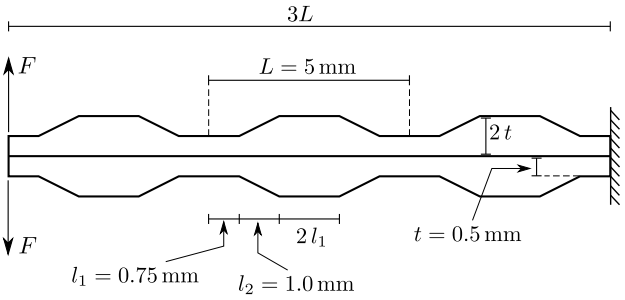

Figure 7: Variable thickness DCB: structural model.

The specimen is fixed at one end by constraining all the degrees of freedom, and is loaded at the other side with two concentrated forces directed as shown in Figure 7. The two parts of the beam are made of isotropic material with a plane strain constitutive law. The material is characterized by a Young's modulus equal to 70000 MPa and a Poisson's ratio of 0.3.
The finite element model consists of 474 two-dimensional continuum elements, and a layer of 66 cohesive elements is introduced to separate the upper and the lower part of the specimen. The properties of the cohesive constitutive law are summarized in Table 4, while the finite element model is presented in Figure 8.

G_I (Nmm^{-1})	N (N)	k_d (Nmm^{-3})
$5.0 \cdot 10^{-1}$	30.0	$1.0 \cdot 10^{4}$

Table 4: Variable thickness DCB - properties of the cohesive constitutive law.

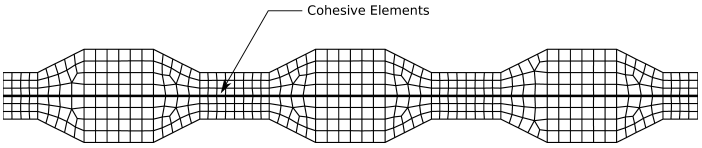

Figure 8: Variable thickness DCB: finite element mesh.

To avoid the premature stop of the analyses and, at the same time, guarantee accurate results, the tolerance is set at $6.0 \cdot 10^{-2}$ for all the solution procedures here investigated. The termination criterion is based on the number of load increments, chosen to ensure that the simulations are arrested when the vertical displacement of the loaded nodes is close to the reference values of 1.8 mm. The parameters adopted in the numerical analyses are reported in Table 5.

Method	$\Delta\lambda_0$	Δl_0 (mm)	Δl_{max} (mm)	$\Delta\tau_0$ (Nmm)	$\Delta\tau_{max}$ (Nmm)	ξ_{max}	W_{switch}
HRi	1.0	-	-	-	$1.0 \cdot 10^{-1}$	1.0	-
HC	1.0	1.0	1.0	-	$1.0 \cdot 10^{-1}$	1.0	0.8
DE	2.0	-	-	$1.0 \cdot 10^{-1}$	$1.0 \cdot 10^{-1}$	-	-
Riks	1.0	-	-	-	-	1.2	-

Table 5: Variable thickness DCB - analysis parameters.

The vertical displacement of the loaded nodes is plotted versus the applied force in Figures 9(a) and 9(b).

In particular, the plot of Figure 9(a) displays the results obtained with the DE and the two hybrid methods, while Figure Figure 9(b) reports a comparison between the Riks method and the reference equilibrium path, in this case computed with the HC method. As observed, the response is characterized by the presence of three load peaks separating the loading an the unloading phases. The deformed configuration corresponding to a crack opening of about 2 mm is presented in Figure 10.

The numerical performances of the methods are summarized in Table 6 in terms of number of steps and iterations, step size reductions, and CPU time. All of the methods are able to reach the end of the analysis, therefore the comparison is performed in terms of total CPU time.

Even though the lowest time is associated with the Riks method, it is worth highlighting that the equilibrium path is poorly represented. In particular, the method is unable to capture the two snap-backs experienced by the structure, as illustrated by Figure 9(a). The three other

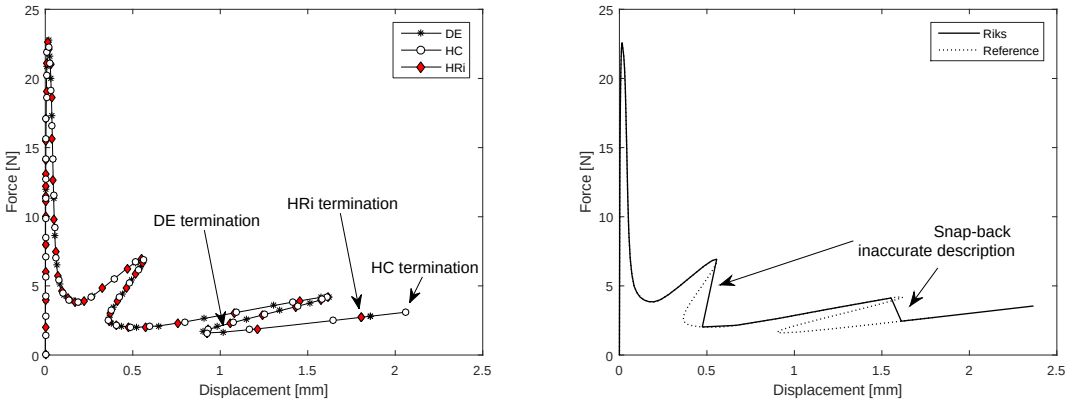

(a) (b)

Figure 9: Variable thickness DCB: (a) comparison between hybrid and DE methods, (b) comparison between Riks and hybrid-Riks methods.

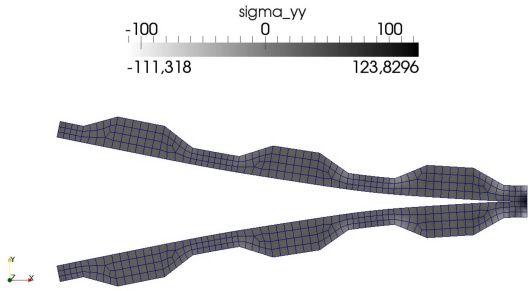

Figure 10: Variable thickness DCB: final deformed configuration.

methods, i.e. the two hybrid strategies and the DE, provide a more complete description of the force-displacement curve, which includes the descending paths after the local peaks. It is worth noting that no beneficial effects could be achieved by reducing the step size of the predictor. A number of parametric studies revealed that, by reducing the value of ξ_{max}, the missing portion of the equilibrium path could be hardly recovered. The lowest CPU time is achieved with the hybrid-Riks method, with a gain of approximately 20% in comparison to the DE approach. Despite the higher number of increments, the HRi method requires 116 iterations versus the 154 of the DE method.

Also the hybrid implementation of the Crisfield method, i.e. HC, guarantees an improved effi-

Method	N. of Incr.	N. of Iter.	N. of Cutbacks	CPU Time (s)
HRi	102	116	0	525
HC	103	124	0	553
DE	80	154	0	629
Riks	49	117	4	485*

Table 6: Variable thickness DCB - numerical performances (*Denotes a poor description of the equilibrium path).

ciency with respect to the DE procedure. In this case, the speed-up is approximately 15%. Even for the HC method, the total number of increments is higher than those performed by the DE approach, while the total number of iterations is smaller.
The results of this example illustrate that the hybrid methods, both in terms of Riks and Crisfield implementation, guarantee improved solution performances in comparison to the purely geometric Riks and the DE approaches. In particular, the presence of three transitions from the loading to the unloading phase is effectively handled by the hybrid solvers, and no successive reductions of the step size are needed as observed for the DE method. Furthermore, the presence of damage-induced snap-backs highlights the inability of the Riks method to properly trace the equilibrium path. In this sense, the hybrid-Riks approach seems to combine the efficiency inherited from the purely geometric Riks strategy and the ability to effectively handle damage phenomena proper of the DE approach.

Perforated Cantilever Beam

The third example deals with the mode I opening of a perforated cantilever beam. The analysis involves the propagation of a discontinuous mode I delamination, and is characterized by alternate elastic and dissipative behaviours.
A sketch of the structure is reported in Figure 11 together with the dimensions and the loading conditions.
The beam is characterized by the presence of five equally spaced holes in the central portion of the structure, and two half holes in outer position. The distance between the holes, measured from center to center, is 80 mm. The total length of the beam is 480 mm, and the width is equal to 40 mm. The structure is fixed at one side and is loaded at the other side with two concentrated forces, as shown in Figure 11. The isotropic material has a plane strain consititutive law with modulus of 1000 MPa and Poisson's ratio of 0.3. To capture the onset and

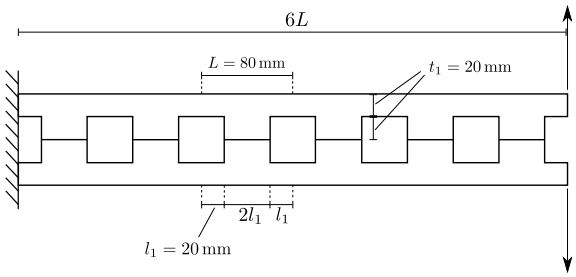

Figure 11: Perforated cantilever beam: structural model.

the propagation of the fracture, a layer of cohesive elements is introduced between the upper and the lower parts of the beam. The properties of the traction-separation constitutive law are provided in Table 7.

G_I (Nmm^{-1})	N (N)	k_d (Nmm^{-3})
$1.0 \cdot 10^{-1}$	1.0	$1.0 \cdot 10^2$

Table 7: Perforated cantilever beam: properties of the cohesive constitutive law.

The finite element model of the structure is composed of 288 two-dimensional continuum elements and 24 cohesive elements, divided into six zones, composed of 4 cohesive elements. A sketch of the model is reported in Figure 12.

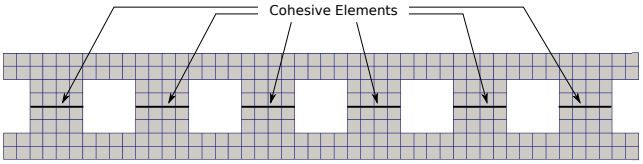

Figure 12: Perforated cantilever beam: finite element mesh.

The parameters of the simulation are reported in Table 8. Based on a preliminary analysis, the tolerance value is equal to $8.0 \cdot 10^{-2}$ for all the methods. The condition $\lambda \geq 20$ is defined as the criterion to terminate the analyses.
The curves relative to the vertical displacement of the loaded nodes are plotted versus the applied load in Figures 13(a) and 13(b).
In particular, Figure 13(a) displays the results obtained using the DE method and the two hy-

Method	$\Delta\lambda_0$	Δl_0 (mm)	Δl_{max} (mm)	$\Delta\tau_0$ (Nmm)	$\Delta\tau_{max}$ (Nmm)	ξ_{max}	W_{switch}
HRi	0.2	-	-	-	$4.0{\cdot}10^{-1}$	1.0	-
HC	0.2	2.0	2.0	-	$4.0{\cdot}10^{-1}$	1.0	0.8
DE	0.2	-	-	$3.0{\cdot}10^{-1}$	$3.0{\cdot}10^{-1}$	-	-
Riks	1.5	-	-	-	-	1.0	-

Table 8: Perforated cantilever beam: analysis parameters.

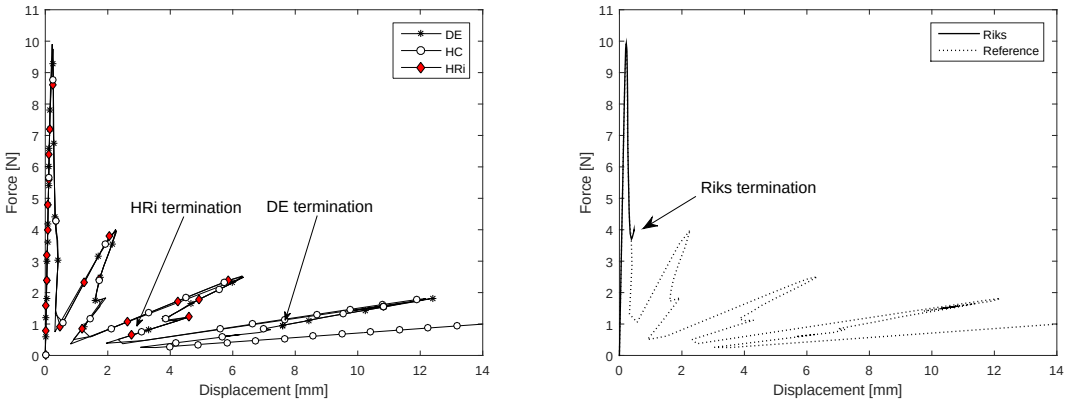

(a) (b)

Figure 13: Perforated cantilever beam: (a) comparison between hybrid and DE methods, (b) comparison between Riks method and reference equilibrium path.

brid approaches, while Figure 13(b) is relative to the results obtained with the Riks method. For clarity purposes, the locations corresponding to the analysis termination observed with the various methods are highlighted in the two figures. The plot illustrates the presence of multiple load peaks followed by abrupt drops due to the opening of the holes. The first peak corresponds to the crack propagation in the first hole, the second peak is relative to the second hole, and so on. As the number of failed holes increases, the reduction of displacement during the unloading phase gets more and more pronounced. Furthermore, the complexity of the response is exacerbated by the presence of a secondary snap-back in the unloading phase. The descending branches of the curves display a partial recovery of the load-carrying capability of the structure, followed by a successive snap-back.

The deformed configuration is reported in Figure 14 as obtained with the HC algorithm when the maximum displacement is approximately 20 mm.

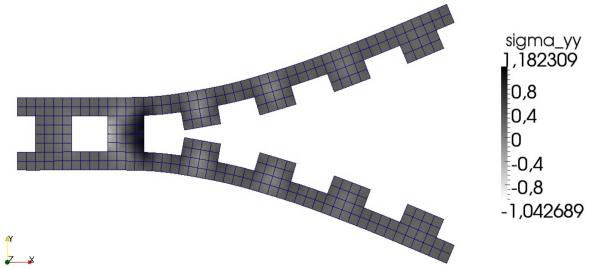

Figure 14: Perforated cantilever beam: final deformed configuration (displacements 5×).

The numerical performances of the methods are compared in Table 9 and are presented in terms of number of load steps, number of iterations, step size reductions and CPU time. Furthermore, the number of fully damaged cohesive elements (i.e. damage variable equal to 1) is proposed as a metric to assess the robustness of the solution methods.

Method	N. of Incr.	N. of Iter.	N. of Cutbacks	N. of Fully-damaged Coh. Els.	CPU Time (s)
HRi	85	103	1	11	201
HC	207	309	13	16	624
DE	91	301	17	13	493
Riks	26	315	19	2	495

Table 9: Perforated cantilever beam - numerical performances (the gray row denotes that the analysis is terminated due to convergence issues).

With this regard, the hybrid-Crisfield method is the one displaying the most interesting features, as the analysis is carried out until the complete failure of 16 cohesive elements, corresponding to the opening of four of the seven holes. Satisfactory results are obtained also for the HRi and the DE methods, which are able to capture large part of the equilibrium branch. For these latest two methods, the total number of fully damaged cohesive elements is equal to 11 and 13, respectively.

The results of Figure 13(b) and Table 9 demonstrate the inability of the purely geometric Riks method to reach convergence after crossing the first peak of load. The step size of the analysis is progressively reduced, until the minimum prescribed value $\xi_{min} = 1.0 \cdot 10^{-3}$ is reached. The

interruption of the analysis coincides with a number of 2 fully damaged cohesive elements, thus demonstrating the difficulties of this method to handle complex responses involving geometric and material nonlinearties.
The efficiency of the methods is compared in terms of CPU time, and the values are reported in the last column of Table 9. It is worth highlighting that the CPU times are referred to the total analysis time, therefore they correspond to equilibrium paths of different length. For instance, the HC method requires 488 s – close to the time needed by the DE method –, but the solution interrupts at a much larger value of the vertical displacement. Nevertheless, the efficiency of the hybrid methods is quite clear, and can be deducted by comparison with the DE method. In particular, the DE method terminates after 493 s, when the number of failed cohesive elements is 13. Contrarily, the HC method guarantees superior performances, as the number of damaged cohesive elements is higher (and equal to 16) in a smaller amount of time. The HRi method terminates the analysis a little bit earlier than the DE method, but the reduction of time is drastic and approximately equal to 60%.
It is then concluded that the hybrid methods can effectively handle a complex nonlinear response, involving both damage phenomena and snap-backs, with improved computational effectiveness with respect to the DE method. At the same time, the example highlights the inability of a purely geometric constraint, as in the case of the Riks method, to guarantee robustness properties when damage phenomena are of concern.

The weighting function γ

To better illustrate the transition from geometric to dissipative constraint, the behaviour of the weighting function is discussed with regard to the example of the perforated beam and considering the hybrid-Crisfield method. The history of the values of γ is plotted in Figure 15 versus the number of increments.
As observed, the parameter γ is initially zero, when the response is purely elastic. At the onset of the dissipative process, the weighting parameter increases from zero to the unitary value with 3 intermediate steps. At this stage the function combines dissipative and geometric requirements. A similar behaviour is observed during the other loading phases. The unloading phases are performed with an abrupt change from γ equal to 1.0 to 0.0. It is worth observing that the transition happens in a very efficient manner, as the possibility of assuming intermediate values of γ is exploited during the iterations at a fixed increment.
By considering a threshold value W_{switch} =0.8 (see Algorithm 1), the roots of the dissipative

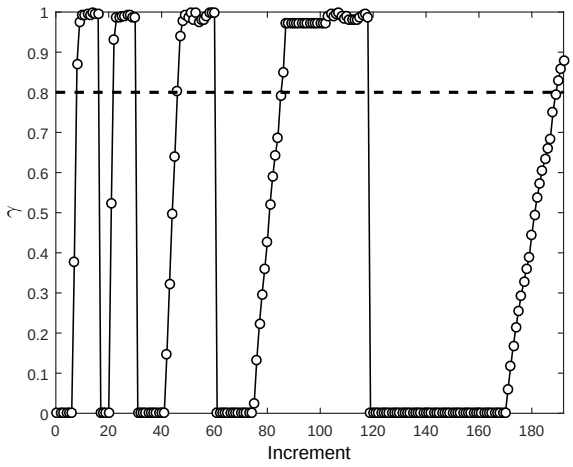

Figure 15: Perforated cantilever beam: history of the values of γ.

branches are traced with the energy-based root selection technique, while the increment direction and the lowest residual methods are used during the unloading phase. The results are illustrated in Figure 16, where the circles denote the transition of the root selection scheme in the context of the force-displacement curve.

5. Conclusions

In this paper, a class of arc-length procedures has been presented for the analysis of geometrically and materially nonlinear problems. The methods make use of a hybrid constraint equation that combines geometric and dissipative requirements by means of a weighted sum. The weight function is automatically updated at each solution step on the basis of the damage state of the structure. The constraint equation is so allowed to vary continuously between the dissipative constraint to the purely elastic one, thus avoiding time-consuming transitions between two distinct solution procedures. The effectiveness of the hybrid-methods has been checked by means of three numerical examples, illustrating good robustness properties and improved computational time. In contrast to the Riks method, the hybrid constraint approaches were able to trace large part of the equilibrium path in all the examples here considered, guaranteeing the convergence even in presence of complex responses involving delaminations and snap-back phenomena. The results illustrated improved computational efficiency with respect to the arc-length procedure based on the coupled use of dissipative constraint and force-control, with total CPU time signif-

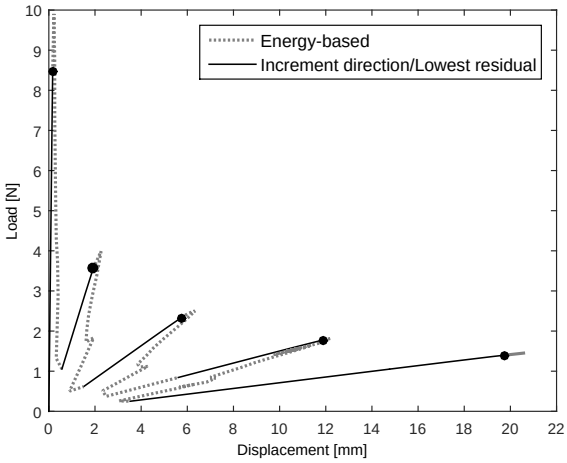

Figure 16: Perforated cantilever beam: root selection schemes in HC.

icantly smaller in all the examples here considered. Regarding the Crisfield implementation of the hybrid approach, a novel root selection criterion was proposed, based on the selection of the root associated with a positive dissipated energy. The validity of the criterion was demonstrated by the absence of solutions characterized by undesired unloading phenomena, that may affects the increment direction and the lower residual methods.

In addition to the good efficiency and robustness properties, an advantage of the hybrid-constraint arc-lengths is their dependence on few algorithmic parameters, thus facilitating the designer to set-up the analysis. The adoption of a mixed dissipative and geometric constraint allows to handle complex responses characterized by alternating geometric and material-dominated events, including elastic or damage-induced snap-backs and snap-throughs. The equilibrium paths can be traced with a high degree of accuracy and no a-priori knowledge of the structural behaviour is needed.

References

[1] E. Riks. The application of Newton's method to the problem of elastic stability. *Journal of Applied Mechanics*, 39(4):1060–1065, 1972.

[2] G.A. Wempner. Discrete approximations related to nonlinear theories of solids. *International Journal of Solids and Structures*, 7(11):1581–1599, 1971.

[3] E. Ramm. *Strategies for tracing the nonlinear response near limit points.* Nonlinear finite element analysis in structural mechanics. Springer-Verlag, 1981.

[4] M.A. Crisfield. A fast incremental/iterative solution procedure that handles "snap-through". *Computers & Structures*, 13(1):55–62, 1981.

[5] M.A. Crisfield. An arc-length method including line searches and accelerations. *International Journal for Numerical Methods in Engineering*, 19(9):1269–1289, 1983.

[6] M. Ritto-Corrêa and D. Camotim. On the arc-length and other quadratic control methods: Established, less known and new implementation procedures. *Computers & Structures*, 86(11):1353–1368, 2008.

[7] M.A. Crisfield. Overcoming limit points with material softening and strain localization. *Numerical Methods for Non-Linear Problems*, pages 244–277, 1984.

[8] I.M. May and Y. Duan. A local arc-length procedure for strain softening. *Computers & Structures*, 64(1):297–303, 1997.

[9] Z. Chen and H.L. Schreyer. A numerical solution scheme for softening problems involving total strain control. *Computers & Structures*, 37(6):1043–1050, 1990.

[10] J.C.J. Schellekens and R. De Borst. A non-linear finite element approach for the analysis of mode-I free edge delamination in composites. *International Journal of Solids and Structures*, 30(9):1239–1253, 1993.

[11] R. De Borst. Computation of post-bifurcation and post-failure behavior of strain-softening solids. *Computers & Structures*, 25(2):211–224, 1987.

[12] J.G. Rots and R. De Borst. Analysis of concrete fracture in "direct" tension. *International Journal of Solids and Structures*, 25(12):1381–1394, 1989.

[13] G. Alfano and M.A. Crisfield. Solution strategies for the delamination analysis based on a combination of local-control arc-length and line searches. *International Journal for Numerical Methods in Engineering*, 58(7):999–1048, 2003.

[14] F. Gasco and P. Feraboli. A crack length control scheme for solving nonlinear finite element equations in stable and unstable delamination propagation analysis. *Composite Structures*, 117:267–273, 2014.

[15] M.A. Gutierrez. Energy release control for numerical simulations of failure in quasi-brittle solids. *Communications in Numerical Methods in Engineering*, 20(1):19–29, 2004.

[16] C.V. Verhoosel, J.J.C. Remmers, and M.A. Gutierrez. A dissipation-based arc-length method for robust simulation of brittle and ductile failure. *International Journal for Numerical methods in Engineering*, 77(9):1290–1321, 2009.

[17] B.A. Memon and X.Z. Su. Arc-length technique for nonlinear finite element analysis. *Journal of Zhejiang University*, 5(5):618–628, 2004.

[18] R. De Borst, M.A. Crisfield, J.J.C. Remmers, and C.V. Verhoosel. *Non-Linear Finite Element Analysis Of Solids And Structures*. John Wiley & Sons, New York, 2012.

[19] H.B. Hellweg and M.A. Crisfield. A new arc-length method for handling sharp snap-backs. *Computers & Structures*, 66(5):705–709, 1998.

[20] S.L. Chan. Geometric and material non-linear analysis of beam-columns and frames using the minimum residual displacement method. *International Journal for Numerical Methods in Engineering*, 26(12):2657–2669, 1988.

[21] P.P. Camanho, C. G. Dávila, and M.F. De Moura. Numerical simulation of mixed-mode progressive delamination in composite materials. *Journal of Composite Materials*, 37(16):1415–1424, 2003.

[22] A. Turon, C.G. Dávila, P.P. Camanho, and J. Costa. An engineering solution for using coarse meshes in the simulation of delamination with cohesive zone models. TM 213547, NASA, 2005.

[23] R. Vescovini, C.G. Dávila, and C. Bisagni. Failure analysis of composite multi-stringer panels using simplified models. *Composites Part B: Engineering*, 45(1):939–951, 2013.

[24] G. Alfano and M.A. Crisfield. Finite element interface models for the delamination analysis of laminated composites: mechanical and computational issues. *International Journal for Numerical Methods in Engineering*, 50(7):1701–1736, 2001.

6. Appendix

$$c_1 = (1-\gamma)\tilde{a_1} \tag{31}$$
$$c_2 = (1-\gamma)\tilde{a_2} + \gamma\tilde{b_2} \tag{32}$$
$$c_3 = (1-\gamma)\tilde{a_3} + \gamma\tilde{b_3} \tag{33}$$

with:

$$\tilde{a_1} = \mathbf{a}_I^T\mathbf{a}_I + \hat{\mathbf{f}}^T\hat{\mathbf{f}} \tag{34}$$
$$\tilde{a_2} = 2\big(\mathbf{a}_I^T\Delta\mathbf{a}_j + \mathbf{a}_I^T\mathbf{a}_{II} + \Delta\lambda_j\hat{\mathbf{f}}^T\hat{\mathbf{f}}\big) \tag{35}$$
$$\tilde{a_3} = \Delta\mathbf{a}_j^T\Delta\mathbf{a}_j + 2\mathbf{a}_{II}^T\Delta\mathbf{a}_j + \mathbf{a}_{II}^T\mathbf{a}_{II} + \Delta\lambda_j^2\hat{\mathbf{f}}^T\hat{\mathbf{f}} - \Delta l^2 \tag{36}$$

and:

$$\tilde{b_2} = \frac{1}{2}\Big(\lambda_0\mathbf{a}_I^T - \mathbf{a}_0^T\Big)\hat{\mathbf{f}} \tag{37}$$
$$\tilde{b_3} = \frac{1}{2}\Big(\lambda_0\Delta\mathbf{a}_j^T\hat{\mathbf{f}} + \lambda_0\mathbf{a}_{II}^T\hat{\mathbf{f}} - \Delta\lambda_j\mathbf{a}_0^T\hat{\mathbf{f}}\Big) - \Delta\tau \tag{38}$$